Neural Extended State Observer Based Command Filtered Back-stepping Hypersonic Vehicle Integrated Guidance and Autopilot

Liang Wang[1], Ke Peng[2], Weihua Zhang[3], Donghui Wang[4]

Authors(1,2,3,4) info: School of Aerospace Science and Engineering, National University of Defense Technology, China, Changsha, DeYa Road 109, KaiFu District, 410073.

Abstract: This paper focuses on the integrated guidance and autopilot design with control input saturation in the end-game phase of hypersonic flight. Firstly, uncertain nonlinear integrated guidance and autopilot model is developed with third actuator dynamics, where the control surface deflection has magnitude constraint. Secondly, neural network is implemented in extended state observer (ESO) design, which is used to estimate the complex model uncertainty, nonlinearity and state coupling. Thirdly, a command filtered back-stepping controller is designed with hybrid sliding surfaces to improve the terminal performance. In the process, different command filters are implemented to avoid the influences of disturbances and repetitive derivation, meanwhile solve the problem of unknown control direction caused by saturation. The stability of closed-loop system is proved by Lyapunov theory, and the principles abided by the controller parameters are concluded through the proof. Finally, series of 6-DOF numerical simulations are presented to show the feasibility and validity of the proposed controller.

Keywords: integrated guidance and autopilot, neural network, extended state observer, command filter, back-stepping control

1 Introduction

Since 1980s, there have been lots of studies on the area of integrated guidance and control (IGC). In the conventional design, the guidance and control system is treated as two separated processes based on different operation frequencies. The outer guidance system creates acceleration or angle of attack command, and the inner control system tracks it. When the two control loops are combined, the original performance objectives are lost and must be recovered. Thus the resulting iterative design may not produce an optimal overall system. Additionally, under the condition of high speed, imprecisely known aerodynamics, complicated uncertainties and external disturbances, the hypersonic flight dynamics is obviously characterized by nonlinearities. The approaches which involves linearization about a set of equilibrium conditions or trim points within the flight envelop suffer from several disadvantages. Comparatively, the IGC design has provided better solutions in low-cost, modular growth, design flexibility, simple logistics and attracted great interest of researchers.

In [1], the scheme of tactical missile IGC system is designed, where information produced by inertial sensors of guidance system are used for the attitude control system. Because the accuracy of sensors in guidance system is much greater than that of autopilot, the IGC can reduce cost and improve the entire guidance and control system performance. In [2], the discussion of IGC scheme goes a step further with three optimal control laws for a tactical missile. In [3, 4], new optimal control methods are proposed to effectively design IGC system for missiles. However, the weighting matrices have too many elements, while the actuator dynamics is assumed sufficiently fast and are not modeled in the IGC development. In comparison, sliding mode control (SMC) is a robust method with not complicated structure for nonlinear control issues. It has been extensively used in IGC design. In [5], a brief review of SMC is made at first. A simple first order actuator dynamics is considered in model development. Then the missile IGC design is compared with two different separated designs. It's indicated that the inherent instability of decoupled guidance and control loops in terminal phase is postponed by the integrated design, so the interception accuracy is greatly improved. Besides, the control input chasing is depressed by using Zero-Error-Miss (ZEM) sliding surface. In [6], Predicted-Impact-Point (PIP) heading error is used to make sliding surface, and terminal second order sliding mode control is designed to achieve the convergence in a finite time without chattering. In [7, 8], the IGC dynamics is built with two first order actuators for dual-control missiles, and the controller complexity becomes staggering. Nevertheless, the true missile dynamics has high order for second or third order actuator dynamics. For high order nonlinear system model in [9-12], back-stepping technique is a useful tool, which is always combined with SMC and disturbance observer. In [9], the nonlinear disturbance observer is implemented to estimate the nonlinearities, uncertainties, disturbances in the system dynamics, thus the decrease of undesired chattering in control is achieved and the robustness of closed-loop system is enhanced. In [10], the ESOs are used to estimate indirectly measured states and various parametric uncertainties. The nonlinear ESO in [11] has better performance under complex uncertainties and measurement noises than linear ESO in [12, 13], however, it has more parameters to tune. In [14], velocity tracking error is used to design a composite-errors-based ESO in a feedback form, which makes estimation and tracking errors smaller without high gains.

Neural network are capable of providing arbitrarily good approximations to prescribed functionals of a finite number of real variables in [15]. Application to dynamic system modeling, nonlinear complex valued signal processing associated with the RBF network are describe in [16]. In [17], direct neural control is proposed to deal with the input nonlinearity in the model of hypersonic vehicle. An adaptive neural network is employed to estimate the structure uncertainties, then back-stepping controller is proposed to guarantee the uniform asymptotic stability of the uncertain system in [18]. In [19], RBF NN approximation is combined with adaptive back-stepping technique to achieve boundedness of all closed-loop system states.In [20], radial basis function neural networks are applied to approximate the lumped unknown nonlinearities to satisfy robustness against system uncertainties for a constrained flexible air-breathing hypersonic vehicle.

In order to simplify the implementation and cancel out the system noises, command filter is introduced. In [21], command filtered back-stepping is proposed to offer a means to get the time derivatives of the pseudo control signals. In [22, 23], low-pass filter is employed to construct the derivative of pseudo control input. It solves the problem of "explosion of complexity" caused by the repeated differentiations of the pseudo control signals in dynamic surface control (DSC). In [24], the second-order command filters instead of the first-order filters are applied in DSC. With the help of command filters, the performance of back-stepping control scheme significantly improves in stability and steady-state tracking accuracy, while the analysis is made in detail in [25]. In [26], the stability of commander filtered back-stepping control is further improved by composite learning. In [27, 28], a second order command filter is designed to impose magnitude and rate limitation on the control input. In [29], directly differentiating the pseudo control command respect to time is avoided and the global uniform ultimate boundlessness of the tracking errors is guaranteed in the presence of the input constraints. In [30], low-pass filters of the adaptive control scheme guarantee the fast adaptive performance and robustness of the missile integrated guidance and autopilot system. Deep discussion about control input constraint, finite time convergence in IGC design arises rapidly in [31-33]. In [34], first order auxiliary dynamics is developed addition to the system model to deal with the input constraints. In [35, 36], Nussbaum function is introduced to compensate for the nonlinear term arising from input saturation and solve the problem of unknown control direction. In [36], a novel Nussbaum gain is proposed for multiple unknown actuator directions and time-varying nonlinearities.

In summary, IGC study should be more focused on the model development with actuator dynamics, coefficients uncertainties and control input constraints. Then, the application is able to be studied and discussed more practically and effectively. Motivated by 1) the integrated guidance and control design, 2) neural network and ESO based disturbance estimate, and 3) command filtered back-stepping control in the presence of control input constraint, this work proposes a novel integrated guidance and autopilot scheme for hypersonic flight.

The paper is organized as follows: In Section 1, the integrated design and related control techniques are introduced. In Section 2, the hypersonic flight dynamics in end game phase with third order actuator model is developed, and the control surface deflection has constraint of magnitude saturation. In Section 3, neural network based ESO is designed to synthetically estimate the uncertainty and time-varying disturbance, and three ESOs are used in different channels of the integrated guidance and autopilot model. In Section 4, the hybrid command filtered back-stepping technique is implemented based on the estimations of ESOs. Hybrid differentiators are used to get the derivate of virtual inputs produced by the sliding mode controllers, and Nussbaum function based command filter is introduced to solve the problem of unknown control direction when differentiating the saturated control input. In Section 5, the stability proof of closed-loop system is given by Lyapunov theory, and the principles followed by the controller parameters are concluded. In Section 6, 6-DOF numerical simulations verify the proposed design with five scenarios, and Monte Carlo simulations are made to test the performance under initial flight states bias and measurement noises. Finally, section 7 concludes the paper.

2 IGA Model

In this section, the integrated guidance and autopilot model in the end-game phase is developed. In Figure 1, the coordinate systems are built without considering the earth rotation. The aerodynamics is built in the velocity coordinate system. V is the velocity of mass center, R is the distance between the mass center and the landing point, q is the angle between line of sight (LOS) and local horizon, γ is the flight path angle, α is the angle of attack (AOA) and δ_z is the control surface deflection. The angle directions shown in Figure 1 are positive.

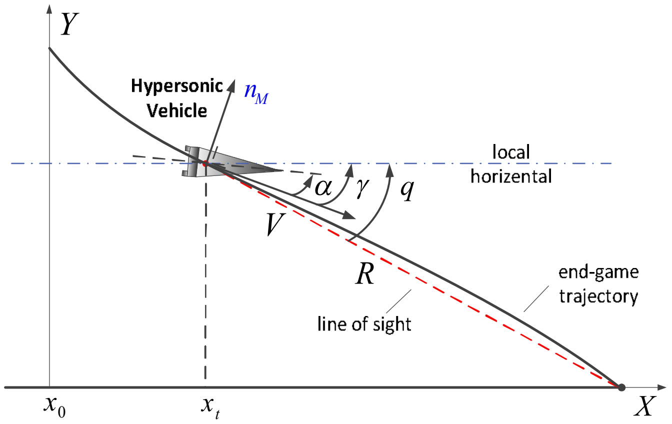

Figure 1. The planar geometry in end-game phase

The state vector is defined as $\boldsymbol{x} = [x_1,\ x_2,\ x_3,\ x_4]^T = [\dot{q},\ \alpha,\ \omega_z,\ \delta_z]^T$, and the control surface deflection is saturated as $v_{act} = sat(x_4)$. Then the state space form of integrated guidance and control system can be depicted as follows:

$$\dot{x}_1 = f_1(x_1) + ax_2 + \Delta f_1(x) + d_1 \tag{1a}$$

$$\dot{x}_2 = f_2(x_2) + x_3 + \Delta f_2(x) + d_2 \tag{1b}$$

$$\dot{x}_3 = f_3(x_2, x_3) + bv_{act} + \Delta f_3(x) + d_3 \tag{1c}$$

where $d_i(t),\ i = 1,\ 2,\ 3$ are the unmatched time-varying disturbances in different channels. The nonlinear functions $f_i(x),\ i = 1,\ 2,\ 3$ and $a,\ b$ are depicted as follows:

$$f_1(x) = -\frac{x_1\dot{R}}{R} + \frac{V}{R}\cos(q-\gamma)\left(x_1 + \frac{g}{V}\cos\gamma - \bar{L}_o\right),\ a = -\frac{V}{R}\cos(q-\gamma)\bar{L}_\alpha \tag{2a}$$

$$f_2(x) = \frac{g}{V}\cos\gamma - \bar{L}_\alpha x_2 - \bar{L}_o \tag{2b}$$

$$f_3(x) = \bar{M}_\alpha x_2 + \bar{M}_\omega x_3,\ b = \bar{M}_{\delta_z} \tag{2c}$$

The lift force can be simplified as two parts: $L = L_\alpha \alpha + L_o$ when the velocity is high. Then $\bar{L}_\alpha = L_\alpha / mV,\ \bar{L}_o = L_o / mV$ in Eq. (2a, 2b) are the unified parts of lift, m is the mass. The aerodynamics moment is also described with two parts: $M_z = M_o + M_{\delta_z}\delta_z$, both are unified by the moment of inertia with respect to body z-axis I_z: $\bar{M}_o = M_o / I_z,\ \bar{M}_{\delta_z} = M_{\delta_z} / I_z$ in Eq. (2c). The high order nonlinearity and states coupling mainly caused by aerodynamics coefficients uncertainties are synthesized as $\Delta f_i(x),\ i = 1,\ 2,\ 3$.

The actuator dynamics is considered as a first order inertial element with time constant τ_{act} and a second order element with damping rate ξ_{act}, natural frequency $\omega_{n,act}$, constant gain K_{act}. Then the transfer function is expressed as following:

$$G_{\delta_z}(s) = \frac{1}{\tau_{act}s + 1}\frac{K_{act}}{s^2 + 2\xi_{act}\omega_{n,act}s + \omega_{n,act}^2} \tag{3}$$

The state space model of actuator can be depicted as follows:

$$\dot{x}_4 = -\frac{1}{\tau_{act}}x_4 + \frac{1}{\tau_{act}}x_{4\tau} \tag{4a}$$

$$\dot{x}_{4\tau} = x_5 \tag{4b}$$

$$\dot{x}_5 = f_{act}(x_{4\tau}, x_5) + b_{act}u + \Delta f_{act}(x_{4\tau}, x_5) + d_{act}(t) \tag{4c}$$

where $f_{act}(x_{4\tau}, x_5)$ is a linear function, $\Delta f(x_{4\tau}, x_5)$ is its uncertain part, and $d_{act}(t)$ is the time-varying disturbance in actuator dynamics. The integrated guidance and autopilot model is developed by Eq. (1) and Eq. (4) with state vector $\boldsymbol{X} = [x_1,\ x_2,\ x_3,\ x_4,\ x_{4\tau},\ x_5]^T$, control input $u = \delta_{zc}$. The nonlinear saturation characteristic of the actuator in Eq. (1c) can be modeled as:

$$sat(x_4) = \begin{cases} \delta_{z,\max}\operatorname{sgn}(x_4), & |x_4| \geq \delta_{z,\max} \\ x_4, & |x_4| < \delta_{z,\max} \end{cases} \tag{5}$$

where $\delta_{z,\max}$ is the magnitude constraint of control surface deflection. The saturated signal can be approximated by a smooth function defined as:

$$g\left(x_4\right)=\delta_{z,\max}\tanh\left(\bar{x}_4\right)=\delta_{z,\max}\frac{e^{\bar{x}_4}-e^{-\bar{x}_4}}{e^{\bar{x}_4}+e^{-\bar{x}_4}},\quad \bar{x}_4=\frac{x_4}{\delta_{z,\max}} \tag{6}$$

then $sat\left(x_4\right)=g\left(x_4\right)+o$, o is the small approximation error.

3 Neural Extended State Observer

As the introduction section refers to, neural network has good approximation performance in dealing with complex system uncertainties and disturbances. In this section, in order to compensate the integrated guidance and autopilot model under complex aerodynamics uncertainties and unmatched disturbances, the technique of neural extended state observer (NESO) is exploited. Firstly, considering the following system:

$$\dot{x}_p\left(t\right)=f_p\left(x_p\right)+b_pu_p\left(t\right)+\Delta f_p\left(x\right)+d_p\left(t\right) \tag{7}$$

The uncertain nonlinearity and time-varying disturbance are considered as a whole $\Delta_p=\Delta f_p\left(x_p\right)+d_p\left(t\right)$ to be estimated. Defining Δ_{eso}, x_{eso} as the states of NESO to estimate respectively Δ_p and x_p, the estimate error of x_p as $e_p=x_{eso}-x_p$, then the state space model of NESO is designed as follows:

$$\begin{cases}\dot{x}_{eso}=f_p\left(x_{eso}\right)+\Delta_{eso}-\beta e_{sys}+b_pu_p\\ \dot{\Delta}_{eso}=\boldsymbol{W}^{*T}\boldsymbol{h}\left(x_{eso}\right)+O\end{cases} \tag{8}$$

where $\boldsymbol{W}^*=\left[w_{11}^*,w_{12}^*,\cdots,w_{1p}^*\right]^T\in\boldsymbol{R}^P$ is the idea weight, $\boldsymbol{h}\left(x_{eso}\right)$ is a vector of Gaussian functions:

$$h_j\left(x_{eso}\right)=\exp\left(-\frac{\left\|x_{eso}-\varepsilon_j\right\|_2^2}{2d^2}\right),\ j=1,2,3,\ldots,n \tag{9}$$

$\boldsymbol{\varepsilon}=\left[\varepsilon_1,\varepsilon_2,\cdots,\varepsilon_n\right]^T$ is the center vector of the Gaussian functions, d is the affect size, and O in Eq.(8) is the construction error of neural network. By employing the σ-modification type of adaptation law, the weight can be functioned as:

$$\dot{\boldsymbol{W}}=\Gamma\left(\boldsymbol{h}e_p-\eta\boldsymbol{W}\right) \tag{10}$$

where $\eta>0$ is constant, $\Gamma>0$ is gain. Defining x_{pr} as reference signal of x_p, then the tracking error can be expressed as $e_p=x_p-x_{pr}$.

In the integrated guidance and autopilot design, three NESOs are used to compensate the unmatched uncertain nonlinearities and time-varying disturbances $\Delta_i=\Delta f_i\left(x\right)+d_i\left(t\right),\ i=1,\ 2,\ 3$ in Eq. (1), the estimate results are respectively $\left[x_{esoi},\ \Delta_{esoi}\right],\ i=1,\ 2,\ 3$.

4 Hybrid Command Filtered Controller

In this section, a hybrid command filtered back-stepping sliding mode controller is designed

Preprints (www.preprints.org) | NOT PEER-REVIEWED | Posted: 16 May 2018 doi:10.20944/preprints201805.0220.v1

to achieve LOS rate convergence based on the estimate results of NESOs.

Step 1: The first sliding surface is chosen as $s_1 = x_1$. The virtual control input $\overline{x}_2$ is designed as reference signal of x_2 according to a proportional reaching law with positive constant k_1.

$$\overline{x}_2 = -\frac{1}{a}\left(k_1 s_1 + \Delta_{eso1}\right) \tag{11}$$

Step 2: Defining the second sliding surface $s_2 = x_2 - x_{2r}$, and the virtual control input $\overline{x}_3$ is obtained by the following control law:

$$\overline{x}_3 = -k_2 s_2 - \Delta_{eso2} + \dot{x}_{2r} \tag{12}$$

where $\dot{x}_{2r}$ is the derivative of $\overline{x}_2$, if directly differentiating $\overline{x}_2$ respect to time, the virtual control input $\overline{x}_3$ is likely to peak. So a low-pass command filter is used to get the derivative:

$$\tau_1 \dot{x}_{2r} + x_{2r} = \overline{x}_2, \ \ x_{2r}(0) = \overline{x}_2(0) \tag{13}$$

In Eq. (13), τ_1 is positive time constant. The error produced by the low-pass filter is defined as $\lambda_1 = x_{2r} - \overline{x}_2$, and λ_1 can be sufficiently small when τ_1 is appropriately set.

Another low-pass filter in the same form of Eq. (13) is used to avoid directly differentiating of $\overline{x}_3$.

$$\tau_2 \dot{x}_{3r} + x_{3r} = \overline{x}_3, \ \ x_{3r}(0) = \overline{x}_3(0) \tag{14}$$

Then the error produced by the low-pass filter can be expressed as $\lambda_2 = x_{3r} - \overline{x}_3$ under appropriate time constant τ_2.

Step 3: In this step, there are two sub-steps to finish the tracking control. Firstly, the virtual control input $\overline{x}_4$ is designed to achieve the convergence of $s_3 = x_3 - x_{3r}$ under the following control law:

$$\overline{x}_4 = -k_3 s_3 - \Delta_{eso3} + \dot{x}_{3r} \tag{15}$$

The third low-pass filter is used to get the first order derivative of $\overline{x}_4$:

$$\tau_3 \dot{x}_{4r} + x_{4r} = \overline{x}_4, \ \ x_{4r}(0) = \overline{x}_4(0) \tag{16}$$

The error between $\overline{x}_4$ and x_{4r} is given as $\lambda_3 = x_{4r} - \overline{x}_4$ under time constant τ_3.

Secondly, if defining $s_4 = g(x_4) - x_{4r}$, then differentiating it respect to time:

$$\dot{s}_4 = \xi \dot{x}_4 - \dot{x}_{4r} \tag{17}$$

where x_4 is also given by a low-pass filter with time constant τ_{act}.

$$\xi = \frac{\partial g(x_4)}{\partial x_4}, \ \ \tau_{act} \dot{x}_4 + x_4 = x_{4c} \tag{18}$$

Then the proportional reaching law with positive constant k_4 is chosen to achieve the convergence of s_4. The control direction is unknown because of ξ, a Nussbaum function

$N(\chi)$ is used to design pseudo control input x_{4u}.

$$x_{4u} = \tau_{act} N(\chi) x_{4uc} \tag{19}$$

$$x_{4uc} = \left(\frac{\xi}{\tau_{act}} x_4 + \dot{x}_{4r} - k_4 s_4 \right) \tag{20}$$

The Nussbaum function is defining with the following properties:

$$\limsup_{s\to\infty} \frac{1}{s} \int_0^s N(\zeta) d\zeta = +\infty \tag{21a}$$

$$\liminf_{s\to\infty} \frac{1}{s} \int_0^s N(\zeta) d\zeta = -\infty \tag{21b}$$

According to the above properties, the following Nussbaum function is implemented:

$$N(\chi) = e^{\chi^2} \cos(\chi) \tag{22}$$

The parameter χ is an adaptive parameter according to the following principle:

$$\dot{\chi} = \gamma_\chi \left(\frac{\xi}{\tau_{act}} x_4 + \dot{x}_{4r} - k_4 s_4 \right) s_4 \tag{23}$$

In the end, a third order differentiator is also used as command filter to get first and second order derivatives of the virtual control input x_{4u}:

$$\begin{aligned} \dot{x}_{CF1} &= x_{CF2} \\ \dot{x}_{CF2} &= x_{CF3} \\ \dot{x}_{CF3} &= \frac{4}{\varepsilon^3} \left(-2^{\frac{5}{3}} \left(|v|^{\frac{1}{3}} \operatorname{sgn}(v) \right) - \left| \varepsilon^2 x_{CF3} \right|^{\frac{5}{3}} \operatorname{sgn}\left(\varepsilon^2 x_{CF3} \right) \right),\ x_{CF1}(0) = x_{4u}(0) \end{aligned} \tag{24}$$

where $v = x_{CF1} - x_{4u} + \left| \frac{1}{\varepsilon} x_{CF2} \right|^{\frac{9}{7}} \operatorname{sgn}(\varepsilon x_{CF2})$, the error between x_{CF3} and x_{4u} can be enough small through choosing suitable ε.

Step 4: The task of tracking x_{4u} is completed by a terminal sliding mode controller. Considering the second order dynamics in Eq. (4b) and Eq. (4c), the uncertainty and the time-varying disturbance are bounded by positive constants F, D.

$$\left| \Delta f_{act} \right| \le F,\ \left| d_{act} \right| \le D \tag{25}$$

Defining error vector $E = \left[e_{act},\ \dot{e}_{act} \right]^T$ with $e_{act} = x_{4\tau} - x_{4u}$, and its derivative can be written as $\dot{e}_{act} = \dot{x}_{4\tau} - x_{CF2}$. Then the following nonlinear sliding mode surface is designed:

$$s_{act} = CE - CP \tag{26}$$

In Eq. (26), $C = [c_1,\ c_2]$ is a constant vector, and $P = [p,\ \dot{p}]^T$ is determined by the following nonlinear function:

$$p(t)=\begin{cases} e_{act}+\dot{e}_{act}t+\frac{1}{2}\ddot{e}_{act}t^2-\left(\frac{10}{T^3}e_{act}+\frac{6}{T^2}\dot{e}_{act}+\frac{3}{2T}\ddot{e}_{act}\right)t^3 \\ +\left(\frac{15}{T^4}e_{act}+\frac{8}{T^3}\dot{e}_{act}+\frac{3}{2T^2}\ddot{e}_{act}\right)t^4-\left(\frac{6}{T^5}e_{act}+\frac{3}{T^4}\dot{e}_{act}+\frac{1}{2T^3}\ddot{e}_{act}\right)t^5,\ 0\le t\le T \\ 0,\ t>T \end{cases} \tag{27}$$

where T is the convergence time of the terminal sliding mode controller.

Finally, the control input is designed as follows:

$$u=-\frac{1}{b_{act}}\left(f_{act}(x)-x_{CF3}-\ddot{p}+\frac{c_1}{c_2}(\dot{e}_{act}-\dot{p})\right)-\frac{1}{b_{act}}\mathrm{sgn}(c_2 s_{act})(F+D) \tag{28}$$

5 Stability Analysis

Defining $e_1=x_1,\ e_2=x_2-\bar{x}_2,\ e_3=x_3-\bar{x}_3,\ e_4=g(x_4)-\bar{x}_4$, and differentiating them with respect to time:

$$\dot{e}_1=\dot{x}_1=-k_1e_1+e_2+\varepsilon_1 \tag{29}$$

$$\dot{e}_2=\dot{x}_2-\dot{\bar{x}}_2=-k_2e_2+e_3+\varepsilon_2+k_2\lambda_1+\dot{\lambda}_1 \tag{30}$$

$$\dot{e}_3=\dot{x}_3-\dot{\bar{x}}_3=-k_3e_3+e_4+\varepsilon_3+k_3\lambda_2+\dot{\lambda}_2 \tag{31}$$

$$\dot{e}_4=x_{4uc}\left(\xi N(\chi)-1\right)-k_4e_4+\dot{\lambda}_3+k_4\lambda_3 \tag{32}$$

Besides the following Lyapunov function is chosen:

$$V=\frac{1}{2}e_1^2+\frac{1}{2}e_2^2+\frac{1}{2}e_3^2+\frac{1}{2}e_4^2+\frac{1}{2}s_{act}^2 \tag{33}$$

Differentiating the actuator dynamics related part of Eq. (33) with respect to time:

$$\begin{aligned} s_{act}\dot{s}_{act}&=\sigma\left\{c_2\left(f_{act}-\ddot{x}_{4u}-\ddot{p}+\frac{c_1}{c_2}(\dot{e}_{act}-\dot{p})\right)+c_2b_{act}u+c_2\left(\Delta f_{act}+d_{act}\right)\right\} \\ &\le s_{act}\left(c_2\left(x_{CF3}-\ddot{x}_{4u}\right)-c_2\,\mathrm{sgn}(c_2s_{act})(F+D)+c_2\left(\Delta f_{act}+d_{act}\right)\right) \\ &\le c_2s_{act}\left(x_{CF3}-\ddot{x}_{4u}\right)-\left|c_2s_{act}\right|(F+D)+c_2s_{act}\left(\Delta f_{act}+d_{act}\right) \end{aligned} \tag{34}$$

Because the differentiator is set appropriately such that $\left|x_{CF3}-\ddot{x}_{4u}\right|\le o_{CF}$, o_{CF} is small positive constant, and $\Delta f_{act},\ d_{act}$ is bounded. We can find a positive constant K to yield to:

$$s_{act}\dot{s}_{act}\le-\mathrm{K}\left|c_2s_{act}\right| \tag{35}$$

Through differentiating Eq. (33) and combining Eq. (34), we have:

$$\begin{aligned} \dot{V}&\le e_1\dot{e}_1+e_2\dot{e}_2+e_3\dot{e}_3+e_4\dot{e}_4+s_{act}\dot{s}_{act} \\ &\le -k_1e_1^2-k_2e_2^2-k_3e_3^2-k_4e_4^2+e_1e_2+e_2e_3+e_1\varepsilon_1 \\ &\quad+e_2\left(\varepsilon_2+\dot{\eta}_1+k_2\eta_1\right)+e_3\left(\varepsilon_3+\dot{\eta}_2+k_3\eta_2\right)+e_4\left(\dot{\eta}_3+k_4\eta_3\right)+x_{4uc}e_4\left[\xi N(\chi)-1\right] \end{aligned} \tag{36}$$

If defining the following bounds:

$$\kappa = \varepsilon_{\max} + k_{\max}\eta_{\max} + \dot{\eta}_{\max} \tag{37a}$$

$$\varepsilon_{\max} = \max\left[\left|\varepsilon_1\right|,\left|\varepsilon_2\right|,\left|\varepsilon_3\right|\right] \tag{37b}$$

$$k_{\max} = \max\left[k_1,k_2,k_3\right] \tag{37c}$$

$$\eta_{\max} = \max\left[\left|\eta_1\right|,\left|\eta_2\right|,\left|\eta_3\right|\right] \tag{37d}$$

$$\dot{\eta}_{\max} = \max\left[\left|\dot{\eta}_1\right|,\left|\dot{\eta}_2\right|,\left|\dot{\eta}_3\right|\right] \tag{37e}$$

According to the Young's inequality, Eq. (36) can be rewritten as following:

$$\dot{V} \le -\left(k_1-1\right)e_1^2 - \left(k_2-\frac{3}{2}\right)e_2^2 - \left(k_3-1\right)e_3^2 - \left(k_4-1\right)e_4^2 + \frac{1}{2}\kappa^2 + x_{4uc}e_4\left[\xi N\left(\chi\right)-1\right] \tag{38}$$

Remark: If choosing $C = \min\left[\left(k_1-1\right),\left(k_2-\frac{3}{2}\right),\left(k_3-1\right),\left(k_4-1\right)\right]$, then the following inequality is yielded to:

$$\dot{V} \le -CV + \frac{1}{2}\kappa^2 + \frac{\dot{\chi}}{\gamma_\chi}\left[\xi N\left(\chi\right)-1\right] \tag{39}$$

Integrating Eq. (39) directly, then we have:

$$V\left(t\right) \le V\left(0\right)e^{-Ct} + \frac{\kappa^2}{2C}\left(1-e^{-Ct}\right) + \frac{e^{-Ct}}{\gamma_\chi}\int_0^t \dot{\chi}\left[\xi N\left(\chi\right)-1\right]e^{C\tau}d\tau \tag{40}$$

According to the proof in [36], $\int_0^t \dot{\chi}\left[\xi N\left(\chi\right)-1\right]e^{C\tau}d\tau$ is bounded, and $V\left(t\right)$ is bounded, which implied all the error is bounded.

6 Numerical Simulation

In this section, series of 6-DOF nonlinear numerical simulations are provided to illustrate the control schemes proposed in the previous sections. Firstly, the initial flight condition in end-game phase is set as follows:

$$\begin{aligned} &R_0 = 20km,\ V = 1200m/s,\ g = 9.8m/s^2 \\ &\alpha_0 = 0\deg,\ \gamma_0 = -10\deg,\ q_0 = -60\deg \end{aligned} \tag{41}$$

The IGA model is built in four scenarios with the following aerodynamics coefficients based on table in Appendix A.

Scenario 1:

$$\begin{aligned} &\bar{L}_\alpha = 1,\ \bar{L}_o = -1.6, \\ &\bar{M}_\alpha = 0.1,\ \bar{M}_\omega = -1,\ \bar{M}_\delta = 1 \end{aligned} \tag{42a}$$

Scenario 2:

$$\begin{aligned} &\bar{L}_\alpha = 1-0.01\alpha,\ \bar{L}_o = -1.6, \\ &\bar{M}_\alpha = 0.1-0.001\alpha,\ \bar{M}_\omega = -1-0.001\omega_z,\ \bar{M}_\delta = 1 \end{aligned} \tag{42b}$$

Scenario 3:

$$\begin{aligned}&\bar{L}_\alpha = 1-0.01\alpha-0.01\delta_{z,sat},\ \bar{L}_o = -1.6,\\&\bar{M}_\alpha = 0.1-0.001\alpha-0.001\delta_{z,sat},\ \bar{M}_\omega = -1-0.001\omega_z,\ \bar{M}_\delta = 1\end{aligned} \tag{42c}$$

Scenario 4:

Furthermore, the un-modeled measurement uncertainty of $\dot{q}$ in Scenario 4 is considered as a first order transfer function:

$$G_{sensor}\left(s\right) = \frac{0.75}{0.05s+1} \tag{42d}$$

The third order actuator dynamics is given by the following transfer function:

$$G_{\delta_z}\left(s\right) = \frac{1}{0.0198s+1}\frac{4621}{s^2+66.34s+4848} \tag{43}$$

Scenario 5:

Dead-zone is also part of control input nonlinearity, which can be defined by Eq. (6) with the following function of $\delta_{z,\max}$:

$$\delta_{z,\max} = \begin{cases}0, & t \le 1\\10, & else\end{cases} \tag{44}$$

The time-varying disturbances in different channels of IGA model are given as follows:

$$d_1 = 0.001\sin\left(2t\right),\ d_2 = 0.05\cos\left(2t\right),\ d_3 = 0.05\sin\left(t\right)\cos\left(2t\right),\ d_{act} = 0.01\sin\left(t\right) \tag{45}$$

Secondly, the three NESOs are set. The first neural network input is chosen as $\left[x_1, x_2, y_{act}\right]$, according to the bound of the states, the following center vector is employed:

$$\varepsilon_1 = \begin{bmatrix}-3 & -2.25 & -1.5 & -0.75 & 0 & 0.75 & 1.5 & 2.25 & 3\\-20 & -15 & -10 & -5 & 0 & 5 & 10 & 15 & 20\\-10 & -7.5 & -5 & -2.5 & 0 & 2.5 & 5 & 7.5 & 10\end{bmatrix} \tag{46}$$

The second neural network input is chosen as $\left[x_2, y_{act}\right]$, according to the bound of the states, the following center vector is employed:

$$\varepsilon_2 = \begin{bmatrix}-20 & -15 & -10 & -5 & 0 & 5 & 10 & 15 & 20\\-10 & -7.5 & -5 & -2.5 & 0 & 2.5 & 5 & 7.5 & 10\end{bmatrix} \tag{47}$$

The third neural network input is chosen as $\left[x_2, x_3, y_{act}\right]$, according to the bound of the states, the following center vector is employed:

$$\varepsilon_3 = \begin{bmatrix}-20 & -15 & -10 & -5 & 0 & 5 & 10 & 15 & 20\\-32 & -24 & -16 & -8 & 0 & 8 & 16 & 24 & 32\\-10 & -7.5 & -5 & -2.5 & 0 & 2.5 & 5 & 7.5 & 10\end{bmatrix} \tag{48}$$

The other parameters of NESOs are set with $\beta = \left[30,\ 30,\ 30\right]$.

Thirdly, the first order command filters have time constants $\tau_1 = \tau_2 = \tau_3 = 0.0198s$. The third order differentiator in Eq. (24) is set with $\varepsilon = 0.04$. The control surface deflection is constraint with $\delta_{z,\max} = 10\deg$, and the Nussbaum function in Eq. (22) is set with $\gamma_\chi = 10^{-6}$. The proportional reaching law of back-stepping sliding mode controller is designed with constants $k_1 = 1.2,\ k_2 = 1.45,\ k_3 = 1.45$. The terminal sliding surface in Eq. (26) is set with $c_1 = 5,\ c_2 = 1$, and the bound of uncertainty and time-varying disturbance in Eq. (28) is given as $F = 10,\ D = 3$.

A. *Nominal Simulation*

The nominal simulation results of Scenario 1 (S1) indicate the feasibility of the proposed method. As Figure 2(a) shows, $\dot{q}$ finally converges to zero under the saturated control surface deflection. In Figure 2(d), the control surface deflection of the proposed method is well constraint under the saturation. The state estimate errors of NESO converge well in very small range, the NESO can estimate the system states with good accuracy, and all the states converge under saturated control surface deflection. The results indicate that the proposed control scheme performs very well.

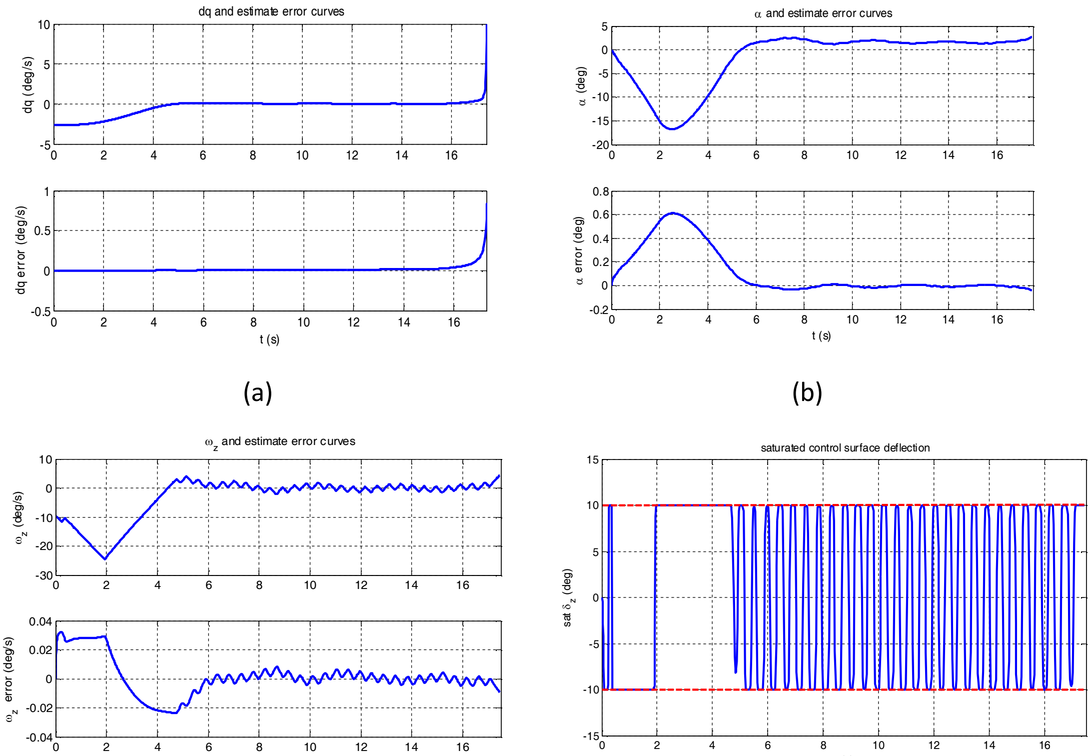

(a) (b)

(c) (d)

Figure 2. IGA and NESO states of Scenario 1: (a) comparison between $\dot{q}$ and NESOI, (b) comparison between α and NESOI, (c) comparison between ω_z and NESOI, and (d) saturated δ_z curve

B. *Comparison Simulations*

Scenario 2 (S2) and Scenario 3 (S3) are set to test the performance under large aerodynamics coefficient uncertainties. In S2, $\bar{L}_\alpha$ in the unified lift force is set with nonlinearity item of AOA, while $\bar{M}_\alpha$, $\bar{M}_\omega$ in the unified moment are also nonlinear functions of AOA and pitch angle rate. In S3, $\bar{L}_\alpha$, $\bar{M}_\alpha$ are influenced by control surface deflection. Besides, simulation in Scenario 4 provides comprehensive testing under complex model uncertainties.

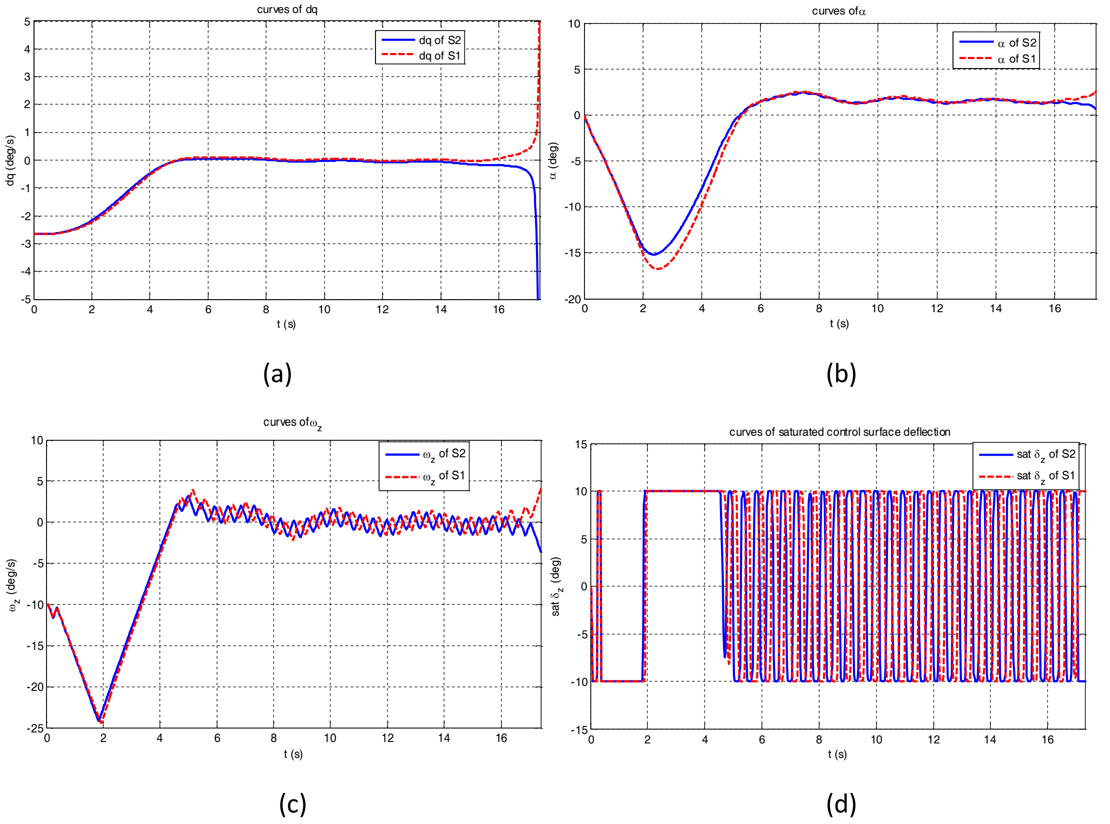

(a) (b)

(c) (d)

Figure 3. Comparison between Scenario 1 and Scenario 2: (a) curves of $\dot{q}$, (b) curves of α, (c) curves of ω_z, and (d) curves of saturated δ_z.

Figure 3 shows the comparison simulation results between S2 and S1. The proposed control scheme is able to cancel out influence of the nonlinear uncertainty in aerodynamics coefficients of lift and moment. Figure 4 shows the comparison simulation results between S3 and S1. The nonlinear parts of control surface deflection in aerodynamics coefficients have a limited impact on the convergence with small overshoot in Figure 4(a) and Figure 4(b). It's indicated that the performance improves under complex nonlinearity with the help of the great approximation ability of neural network.

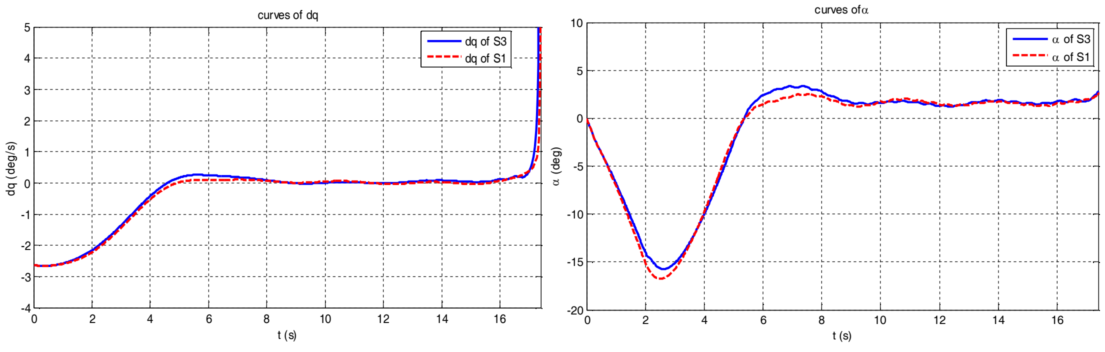

(a) (b)

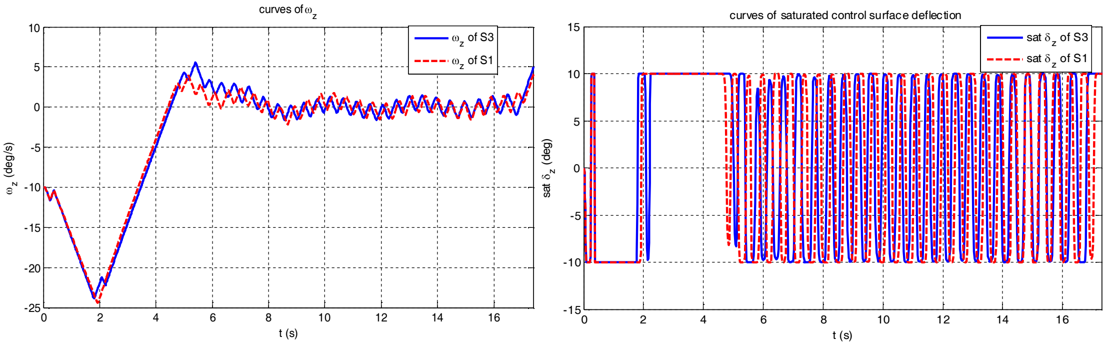

(c) (d)

Figure 4. Comparison between Scenario 1 and Scenario 3: (a) curves of $\dot{q}$, (b) curves of α, (c) curves of ω_z, and (d) curves of saturated δ_z.

The comparison results of S3 and S4 are shown in Figure 5, which indicate that the proposed method can cancel out the complex uncertainties and disturbances with unknown measurement dynamics.

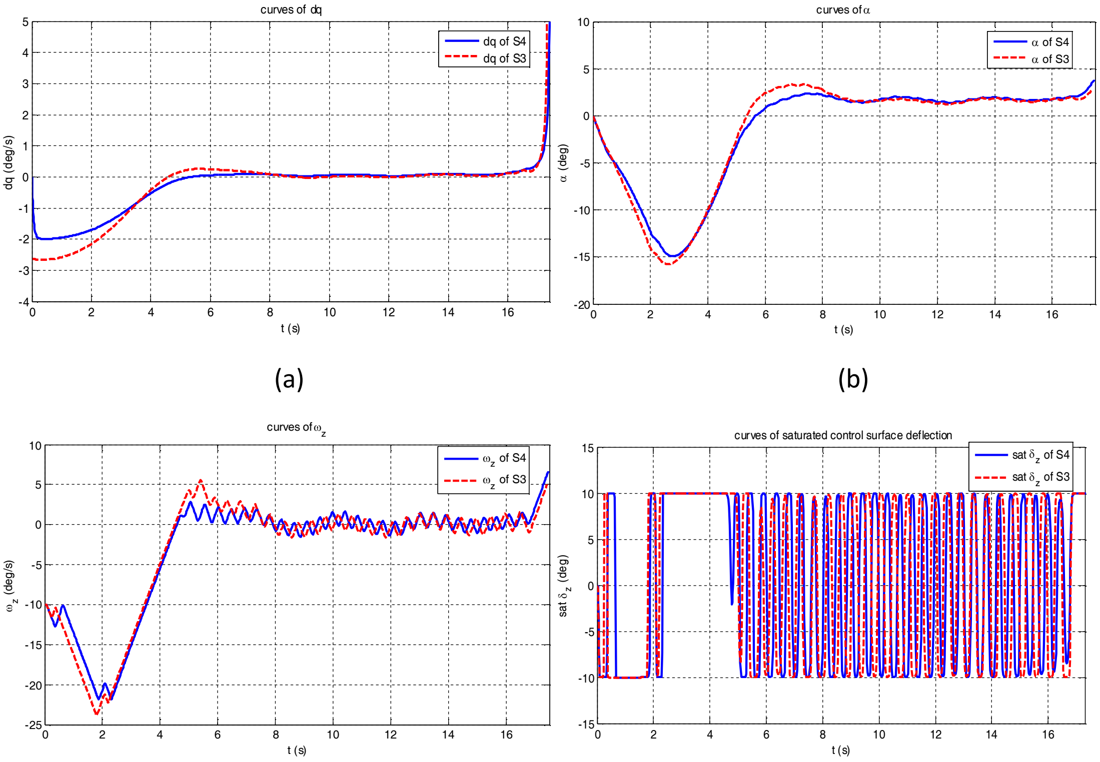

(a) (b)

(c) (d)

Figure 5. Comparison between Scenario 3 and Scenario 4: (a) curves of $\dot{q}$, (b) curves of α, (c) curves of ω_z, and (d) curves of saturated δ_z.

In Figure 6, simulation results in S1 and S5 are compared. Figure 5(d) shows that the control surface deflection of S5 has 1 second dead-zone. It's seen that the NESO approximation based IGA control scheme guarantees the closed-loop system stable under saturated control surface deflection with dead-zone nonlinearity.

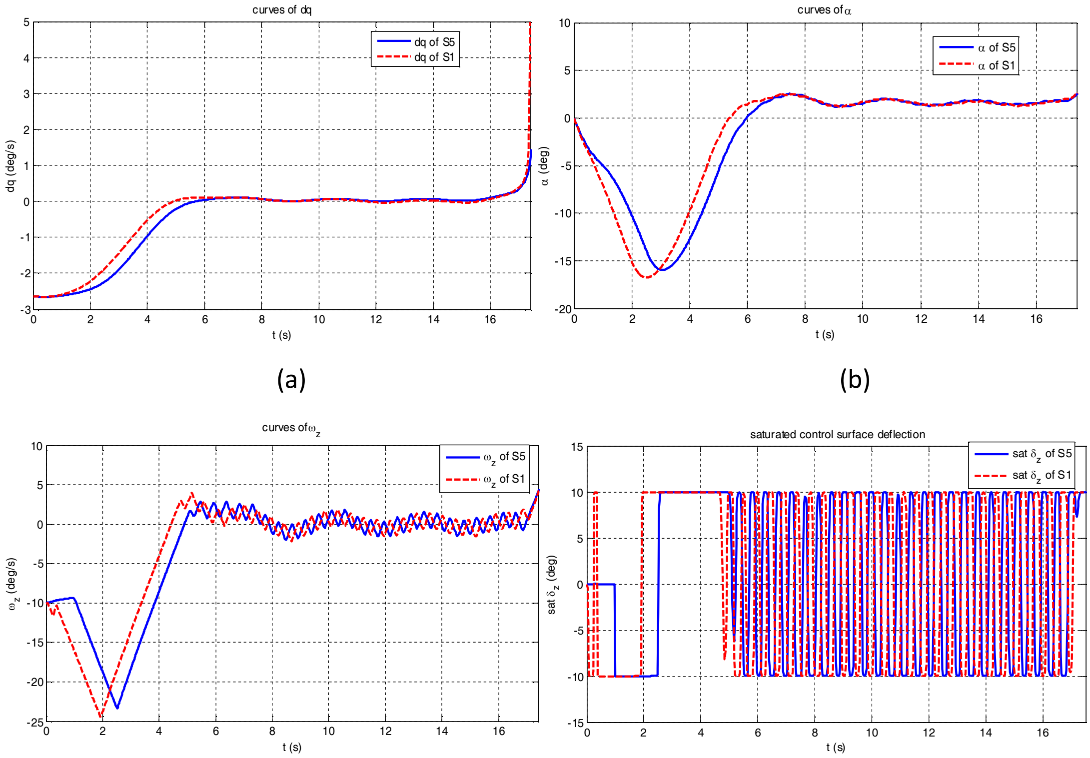

(a) (b)

(c) (d)

Figure 6. Comparison between Scenario 1 and Scenario 5: (a) curves of $\dot{q}$, (b) curves of α, (c) curves of ω_z, and (d) curves of saturated δ_z.

C. *Simulations with Velocity, Initial Distance Dispersion and Measurement Noises*

With the help of Monte Carlo theory, large number of numerical simulations under a wide dispersion range of velocity, initial distance and measurement noises are made. The results are shown in Figure 7, 8, 9. In Figure 7, the simulation results under velocity dispersion between 1000 m/s and 1400 m/s are presented. The mean value is 1200 m/s. It is seen that the parameters setting of the proposed controller can satisfied large variations of flight velocity.

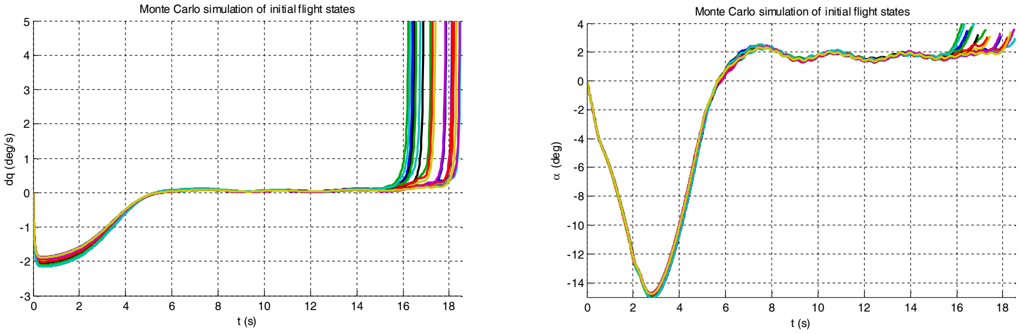

(a) (b)

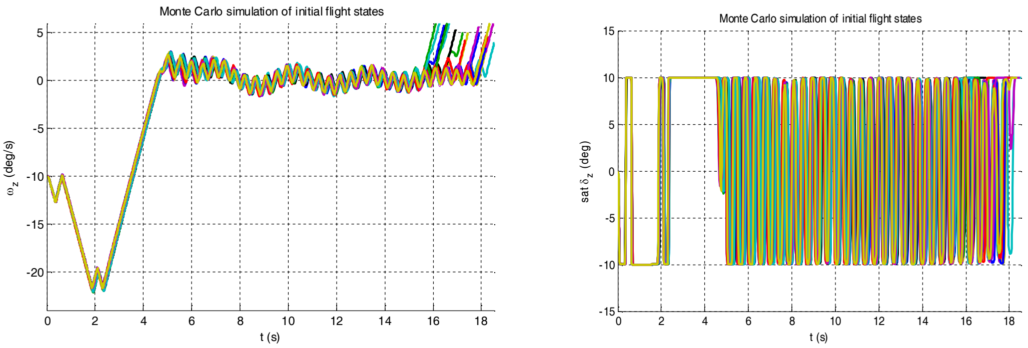

(c) (d)

Figure 7. Monte Carlo Simulation under V dispersion: (a) curves of $\dot{q}$, (b) curves of α, (c) curves of ω_z, and (d) curves of saturated δ_z.

Figure 8 presents the Monte Carlo simulation results under initial distance dispersion between 18km and 22km. The mean value is 20km. It can be seen that the corresponding flight states converge well, the main difference lies in the convergence time under initial distance dispersion. Briefly, the proposed scheme is able to achieve the control object under large dispersion of initial flight states.

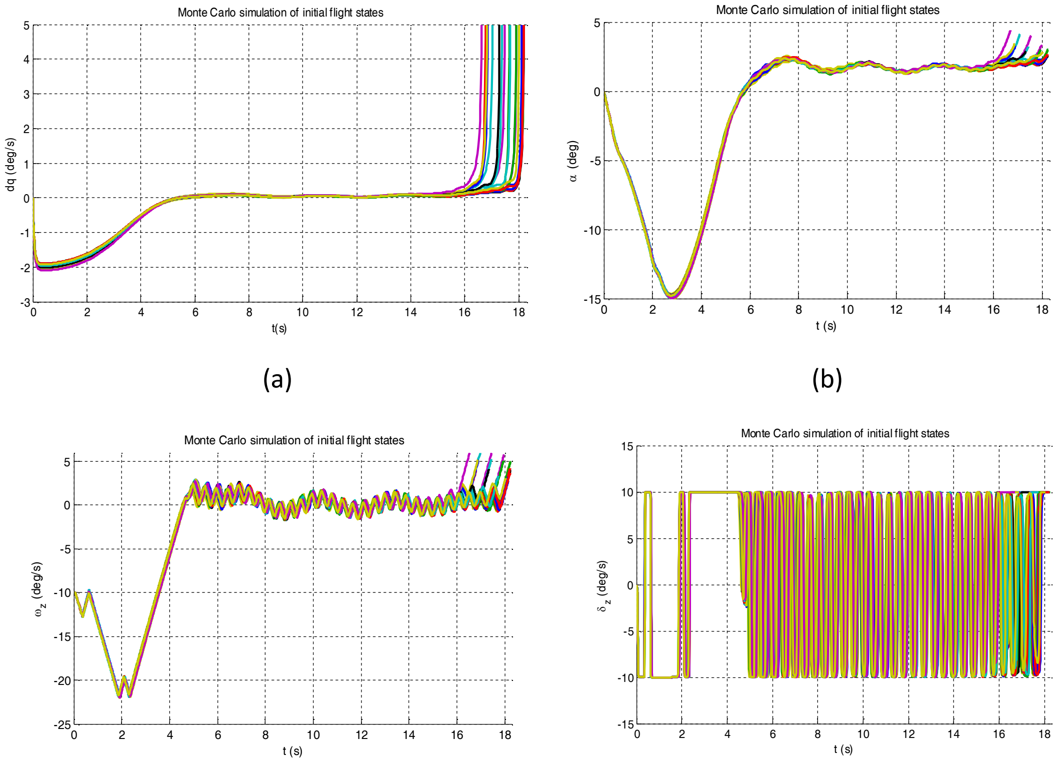

(c) (d)

Figure 8. Monte Carlo Simulation under R_0 dispersion: (a) curves of $\dot{q}$, (b) curves of α, (c) curves of ω_z, (d) curves of saturated δ_z.

In Figure 9, the Monte Carlo simulation results under measurement noises with unknown gain and time constant in Eq. (42d) are presented. It can be concluded that the uncertain gain of sensor dynamics has a very limited effect on the proposed controller.

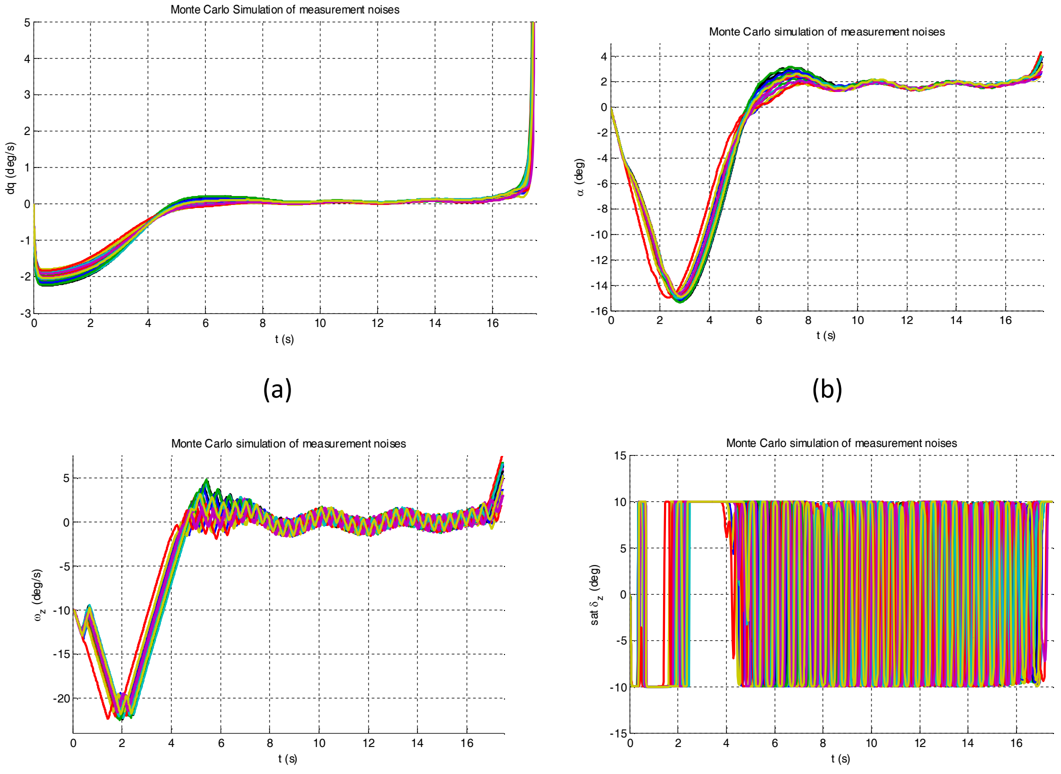

(a) (b)

(c) (d)

Figure 9. Monte Carlo simulation under measurement noises: (a) Curves of $\dot{q}$, (b) Curves of α, (c) Curves of ω_z, (d) Curves of saturated δ_z.

7 Conclusion

In this paper, a novel composite IGA scheme combined with third order actuator dynamics under control input saturation and extended state observer is developed to address hypersonic flight control with multiple uncertainties and control constraint. The complex nonlinearities and unmatched time-varying disturbances are well estimated by three neural ESOs. Four differentiators include a third order hybrid nonlinear differentiator is employed to calculate the derivatives of virtual control input. Thus, the peaking phenomenon and chasing of back-stepping sliding mode controller is greatly depressed. Besides, the noteworthy feature of the proposed IGC approach is that the control surface deflection is constraint under saturation with Nussbaum gain. It is very important in practical application.

References

1. Douglas E. Williams, Jack Richman, Bernard Friedland. (1983). “Design of an integrated strapdown guidance and control system for a tactical missile.” AIAA Guidance and Control Conference, Gatlinburg, TN, USA.

2. Johnny H. Evers, James R. Cloutier. (1992). “Application of integrated guidance and control schemes to a precision guided missile.” American Control Conference, Chicago, IL, USA.

3. Ming Xin, S.N. Balakrishnanm, Ernest J. Ohlmeyer. (2006). “Integrated guidance and control of missiles with θ-D method.” IEEE Transactions on Control Systems Technology, 14(6): 981-992.

4. S.S. Vaddi, P. K. Menon. (2009). "Numerical State-Dependent Riccati equation approach for missile integrated guidance and control." Journal of Guidance, Control, and Dynamics, 32(2): 699-703.

5. Tal Shima, Moshe Idan, Ode M. Colan. (2006). "Sliding mode control for integrated missile autopilot guidance." Journal of Guidance, Control, and Dynamics, 29(2): 250-260.

6. Nathan Harl, S.N. Balakrishnan, Craig Phillips. (2010). "Sliding mode integrated missile guidance and control." AIAA Guidance, Navigation, and Control Conference, Toronto, Ontario Canada.

7. Tal Shima, Moshe Idan, Oded M. Golan. (2007). "Integrated sliding mode Autopilot-Guidance for Dual-Control Missiles." Journal of Guidance, Control, and Dynamics, 30(4): 1081-1089

8. Christian. H. Tournes, Yuri B. Shtessel. (2008). "Integrated guidance and autopilot for dual controller missiles using higher order sliding mode controllers and observers." AIAA Guidance, Navigation and Control Conference and Exhibit, Honolulu, Hawaii.

9. Jian Huang, Songhyok Ri, LeiLiu, etc. (2015). "Nonlinear disturbance observer-based dynamic surface control of mobile wheeled inverted pendulum." IEEE Transaction on Control Systems Technology, 23(6):2400-2407.

10. Qing Guo, Yi Zhang, Branko G. Celler, etc. (2016). "Back-stepping control of electro-hydraulic system based on extended-state-observer with plant dynamics largely unknown." IEEE Transaction on Industrial Electronics, 63(11):6909-6919.

11. Y. Xia, Z. Zhu, M. Fu. (2009). "Back-stepping sliding mode control for missile systems based on an extended state observer." IET Control Theory and Applications, 5(1): 93-1002.

12. Shao Xingling, Wang Honglun. "Back-stepping active disturbance rejection control design for integrated missile guidance and control system via reduced-order ESO." ISA Transactions (2015), http://dx.doi.org/10.1016/j.isatra.2015.01.013.

13. Shao Xingling, Wang Honglu. (2015). "Trajectory linearization control based output tracking method for nonlinear uncertain system using linear extended state observer." Asian Journal of Control, 17(6):1-12.

14. Tairen Sun, Jun Zhang, Yongping Pan. (2017). "Active disturbance rejection control of surface vessels using composite error updated extended state observer." Asian Journal of Control, 19(6):1-10.

15. J. Park, I. W. Sandberg. (1991). "Universal approximation using radial basis function networks." Neural Computation, 3(1991):246-257.

16. Yue Wu, Hui Wang, Biaobiao Zhang, etc. (2012). "Using radial basis function networks for function approximation and classification." International scholarly research network applied mathematics, 2012:1-34.

17. Bin Xu. (2015). "Robust adaptive neural control of flexible hypersonic flight vehicle with dead-zone input nonlinearity." Nonlinear Dynamics, 80(2015):1509-1520.

18. Yuchao Wang, Hansheng Wu. (2015). "Adaptive robust backstepping control for a class of uncertain dynamical systems using neural networks."

19. Bing Chen, Huaguang Zhang. (2016). "Observer based adaptive neural network control for nonlinear systems in nonstrict-feedback form." IEEE Transactions on Neural Networks and

Learning Systems, 27(1):89-98.

20. Xiangwei Bu, Xiaoyan Wu, Daozhi Wei, etc. (2016). “Neural approximation based robust adaptive control of flexible air-breathing hypersonic vehicles with parametric uncertainties and control input constraints.” Information Sciences, 347(2016):29-43.

21. Jay A. Farrell, Marios Polycarpou, Manu Sharma, etc. (2008). “Command filtered backstepping.” American Control Conference, Seattle, Washington, USA.

22. Mingzhe Hou, Guangren Duan. (2011). “Adaptive dynamic surface control for integrated missile guidance and autopilot.” International Journal of Automation and Computing, 8(1):122-127.

23. Xiaoling Liang, Mingzhe Hou, and Guangren Duan. (2014). “Adaptive dynamic surface control for integrated missile guidance autopilot in the presence of input saturation.” Journal of aerospace engineering, 28(5):0414121.

24. Yongping Pan, Huiming Wang, Xiang Li, etc. “Adaptive command-filtered back-stepping control of robot arms with compliant actuators”, IEEE Transactions on Control Systems Technology (2017), DOI:10.1109/TCST.2017.2695600.

25. Yongping Pan, Haoyong Yu. (2015). “Dynamic surface control via singular perturbation analysis.” Automatica, 57(2015):19-33.

26. Yongping Pan, Haoyong Yu. (2016). “Composite learning from adaptive dynamic surface control”, IEEE Transactions on Automatic Control, 61(9):2603-2609.

27. Jay Farrell, Marios Polycarpou, Manu Sharma. (2006). “Adaptive back-stepping with magnitude, rate, and bandwith constraints: Aircraft longitude control.” Air Force Research Laboratory, Wright Patterson AFB, OH, 45433.

28. Bin Xu, Shixing Wang, Daoxiang Gao, etc. (2014). “Command filter based robust nonlinear control of hypersonic aircraft with magnitude constraints on States and Actuators.” Journal of Intelligent Robot System, 73:233-247.

29. Dongkyoung Chwa. (2011). “Global tracking control of under-actuated ships with input and velocity constraints using dynamic surface control method”, IEEE Transaction on Control Systems Technology, 19(6):1357-1370.

30. David Erdos, Tal Shima, Evgeny Kharisov, etc. (2012). “L1 adaptive control integrated missile autopilot and guidance.” AIAA Guidance, Navigation, and Control Conference, Minneapolis, Minnesota.

31. Xianghua Wang, Jinzhi Wang. (2013). “Partial integrated missile guidance and control with finite time convergence.” Journal of Guidance, Control, and Dynamics, 36(5): 1399-1409.

32. Xianghua Wang, Jinzhi Wang. (2014). “Partial integrated guidance and control with input constraints and impact angle.” AIAA Guidance, Navigation, and Control Conference, National Harbor, Maryland.

33. Shi Li-nan, Fu Wenxing, Yan Jie. (2010). “Investigation on the impact of non-linear factors of missile rudders on high-accuracy attitude control.” Journal of Spacecraft TT&C Technology, 29(1):55-59

34. Changyun Wen, Jing Zhou, Zhitao Liu, Hongye. (2011). “Robust adaptive control of uncertain nonlinear systems in the presence of input saturation and external disturbance.” IEEE

Transactions on Automatic Control, 56(7):1672-1678.

35. Ci Chen, Zhi Liu, Yun Zhang, etc. (2015). “Adaptive control of robotic systems with unknown actuator nonlinearities and control directions.” Nonlinear Dynamics, 81:1289-1300.

36. Ci Chen, Zhi Liu, Yun Zhang, etc. (2016). “Saturated Nussbaum function based approach for robotic systems with unknown actuator dynamics.” IEEE Transactions on Cybernetics, 46(10):2311-2321.

Appendix A

The aerodynamics of NASA CAV-L in 1998 is performed in the following table:

AOA	Mach3.5	Mach 5	Mach 8	Mach 15	Mach 20	Mach 23
10°	0.3401	0.3264	0.3108	0.2856	0.2760	0.2739
15°	0.5786	0.5358	0.4883	0.4491	0.4349	0.4319
20°	0.7975	0.7291	0.6731	0.6137	0.5975	0.5966

Table A.1 CAV Lift Coefficient (C_L)

AOA: Angle of Attack. Mach: Mach number

When the flight velocity is high， the lift coefficient can be simplified as $C_L = C_L^{\alpha} \bullet \alpha + C_{L0}$.

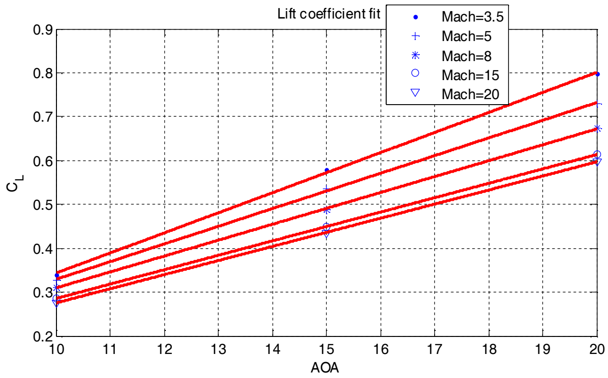

Figure A.1 Polynomial fit results

Mach	C_L^{α}	C_{L0}
3.5	0.04574	-0.114
5	0.04027	-0.07362
8	0.03623	-0.05272
15	0.03281	-0.04268
20	0.03215	-0.4612

Table A.2 Fit curve parameters

Take $Mach = 4,\ H = 20km$ and $S_{ref} = 0.35m^2$ as example to calculate the aerodynamics parameters:

$$\bar{L}_o = \frac{L_o}{mV} = \frac{1}{2}\rho V S_{ref} C_{Lo} = -1.673$$

$$\bar{L}_\alpha = \frac{L_\alpha}{mV} = \frac{1}{2}\rho V S_{ref} C_L^\alpha = 0.9149$$